Supplementary Information

# Initiation of Dendritic Failure of LLZTO via Sub-Surface Lithium Deposition

Marco Siniscalchi[1,2*], Yifu Shi[1], Guanchen Li[3], Joshua S. Gibson[1,2,4], Robert S. Weatherup[1,2], Ruy S. Bonilla[1], Susannah C. Speller[1] and Chris R. M. Grovenor[1,2*]

[1]Department of Materials, University of Oxford, Oxford, OX1 3PH, UK.
[2]The Faraday Institution, Didcot, OX11 0RA, UK.
[3]James Watt School of Engineering, University of Glasgow, Glasgow, G12 8QQ, UK.
[4]Oxford Centre for Energy Materials Research, Henry Royce Institute, Oxford, OX1 3PH, UK.

*Corresponding author(s). E-mail(s):
marco.siniscalchi@materials.ox.ac.uk;
chris.grovenor@materials.ox.ac.uk;

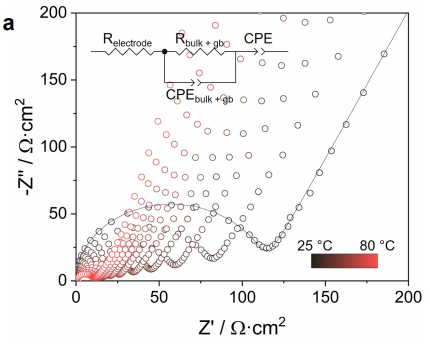


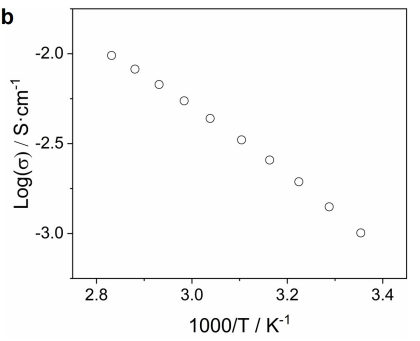


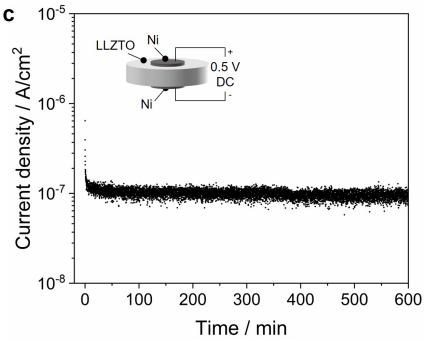


d

**Pellet conductivities at 30 °C**

| Sintering T | $\sigma_{Li^+}$ mS cm$^{-1}$ | $\sigma_{e^-}$ S cm$^{-1}$ |
|---|---|---|
| 1000 °C | 1.36 | $2.19 \cdot 10^{-8}$ |
| 1100 °C | 1.38 | $2.04 \cdot 10^{-8}$ |
| 1200 °C | 1.41 | $1.93 \cdot 10^{-8}$ |

**Supplementary Fig. 1. Ionic and electronic conductivity of LLZTO. a**, Typical electrochemical impedance spectra at various temperatures for a LLZTO pellet with Ni blocking electrodes. The inset shows the equivalent circuit model used to fit the spectra. **b**, Typical Arrhenius plot for the LLZTO pellets used in this study. **c**, Chronoamperometry experiment for a LLZTO pellet with Ni blocking electrodes. 0.5 V is applied to the cell and the steady-state current is measured to evaluate the electronic conductivity. **d**, Ionic and electronic conductivities of LLZTO pellets sintered at different temperatures, i.e. with different densities as shown in Supplementary Fig. 2d.

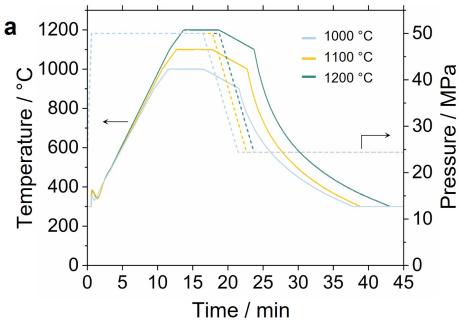


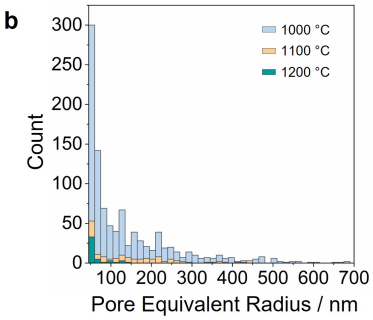


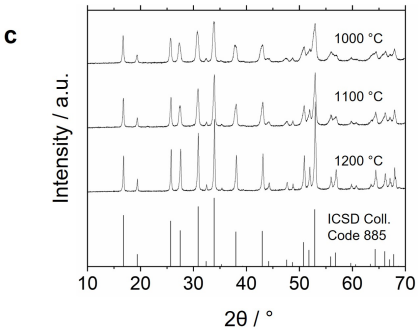


**d**

**Pellet densities (%)**

| Sintering T | SEM | Archimedes |
|---|---|---|
| 1000 °C | 99.2 | 92.3 |
| 1100 °C | 99.89 | 97.4 |
| 1200 °C | 99.99 | 99.4 |

**Supplementary Fig. 2. Spark plasma sintering of LLZTO with different densities.** **a**, Spark plasma sintering temperature and pressure curves. **b**, Porosity analysis based on the SEM surface images in Supplementary Fig. 13a. **c**, X-Ray diffraction (XRD) patterns for different sintering temperatures. Higher sintering temperatures produce sharper XRD peaks, but the lattice structure and purity remain unchanged. **d**, Pellet densities extracted from the images in Supplementary Fig. 13a or from the Archimedes method.

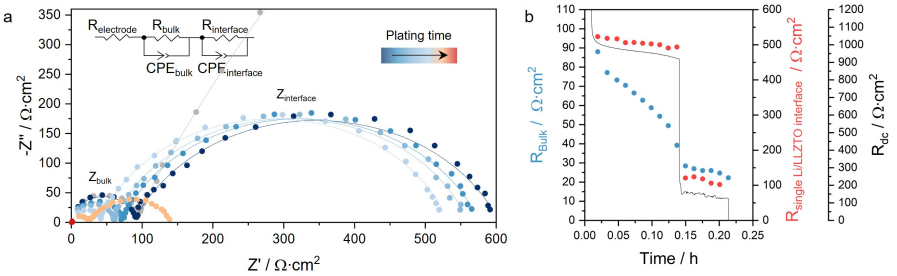


**Supplementary Fig. 3. Galvanostatic impedance spectroscopy during cycling of a Li/LLZTO/Li cell. a**, Extended GEIS data for the cell shown in Figs. 1a and 1b in the manuscript. GEIS spectra were collected before plating (grey •) and every 20 seconds during lithium plating (blue to red •) and were fitted with the equivalent circuit model in the inset. **b**, The fitted $R_{bulk}$ and $R_{int}$ are compared to the DC resistance of the cell. $R_{bulk}$ gradually decreases due to the deposition of lithium in LLZTO, either as lithium dendrites or as isolated lithium deposits. The initial decrease in $R_{int}$, although relatively smaller than that of $R_{bulk}$, can be explained by the improving of Li/LLZTO contact as a result of lithium deposition. The cell short-circuit is visible as sudden voltage drop. For this cell a partial short-circuit occurred around 0.14 h, before a complete cell failure.

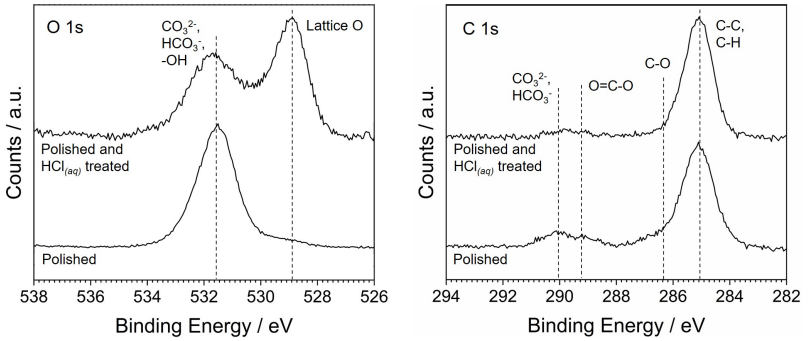


**Supplementary Fig. 4**. **X-ray photoelectron spectroscopy of LLZTO.** O 1s and C 1s XPS signals from the surface of LLZTO, showing that a simple polishing step in the glovebox ($< 0.1$ ppm of $O_2$ and $H_2O$) is not enough to remove the surface contamination. Instead, if the polished LLZTO pellet is acid treated (10 seconds in 1 M $HCl_{(aq)}$), the signal from carbonate and hydroxide species decreases and the LLZTO lattice oxygen signal appears.

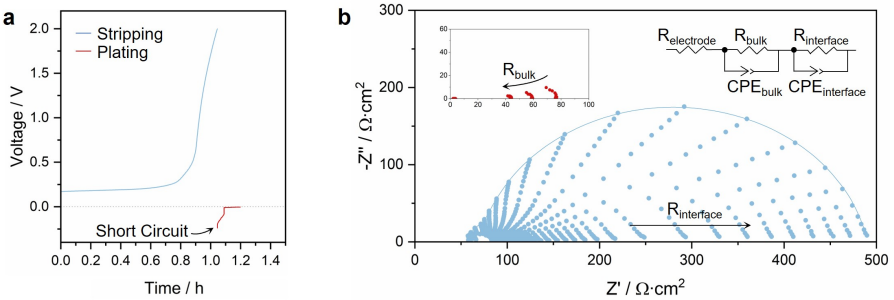


**Supplementary Fig. 5. Cycling of a Li/LLZTO/Li cell with near-zero starting $\mathbf{R}_{int}$.** **a**, Voltage profile for the stripping and plating of a Li/LLZTO/Li cell where the LLZTO was subjected to acid treatment prior to cell assembly in order to remove the lithio-phobic surface contaminants and obtain a near zero starting $R_{int}$ (4 Ω cm$^{-2}$). The cell was cycled at 2 mA cm$^{-2}$ and 5 MPa of stack pressure. **b**, Galvanostatic impedance spectra were taken at constant intervals during cycling and show a large increase in $R_{int}$. This results in the cell polarization visible in **a**. A short circuit immediately occurs upon switching the current sign, as lithium dendrites grow from the plating electrode into the LLZTO pellet. During this process, the bulk impedance decreases as shown in the inset.

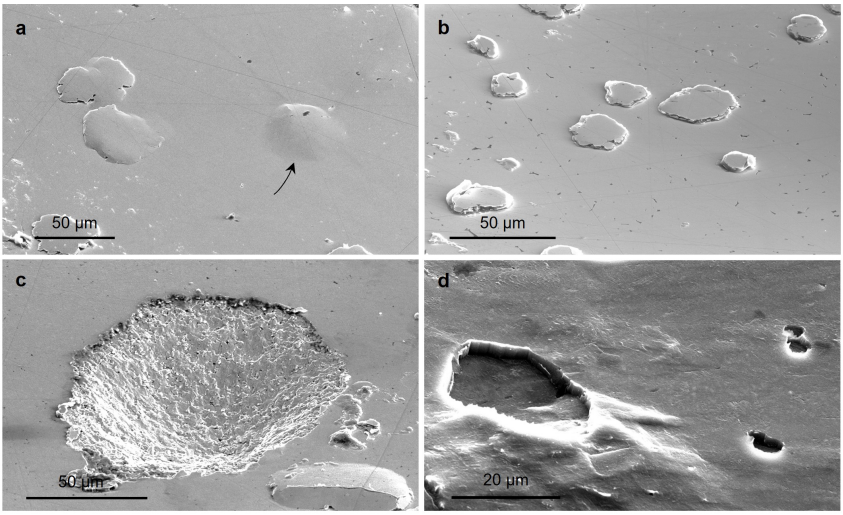


**Supplementary Fig. 6**. **Secondary electron images of surface spallations. a** and **b**, Spallation cracks revealed on the surface of LLZTO after the Li/LLZTO/Li cell was short circuited by a lithium dendrite and the plated Li-WE was peeled off. Notice how one spallation in **a** (arrowed) has not cracked to the LLZTO surface yet. **c**, Peeling the Li-WE off can damage some cracks and remove the fractured LLZTO, in particular for large spallations, leaving a crater behind. **d**, Surface of the Li-WE showing indentations left by the fractured LLZTO, which is pushed into the soft electrode by the lithium freshly plated in the spallation crack.

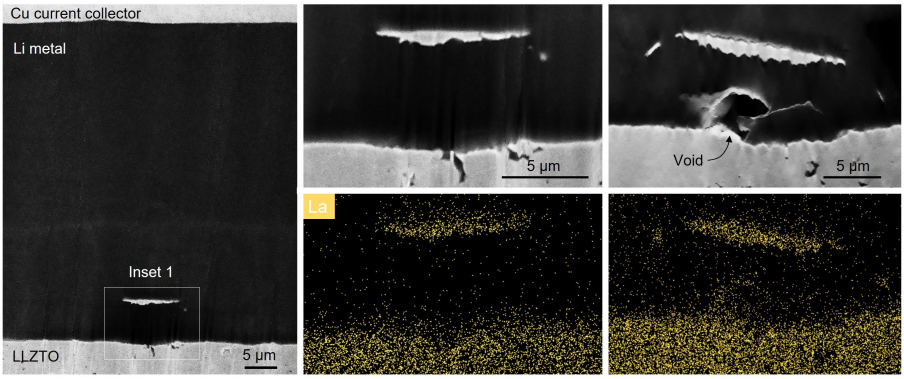


**Supplementary Fig. 7. Spallation cracks at the buried Li/LLZTO interface**. Secondary electron and EDS images of spallation cracks visible after lithium plating at the Li/LLZTO interface, which was cross-sectioned with plasma-FIB without peeling the lithium electrode off. The location of the fractured LLZTO cap is confirmed by the La maps. This suggests that peeling off the lithium electrode introduces no or little mechanical damage, while it allows an easier access to the LLZTO surface. In the spallation crack on the right, the Li-WE could not deform quickly enough to accommodate the freshly plated lithium, so that the plated lithium is not fully dense and a void can be seen.

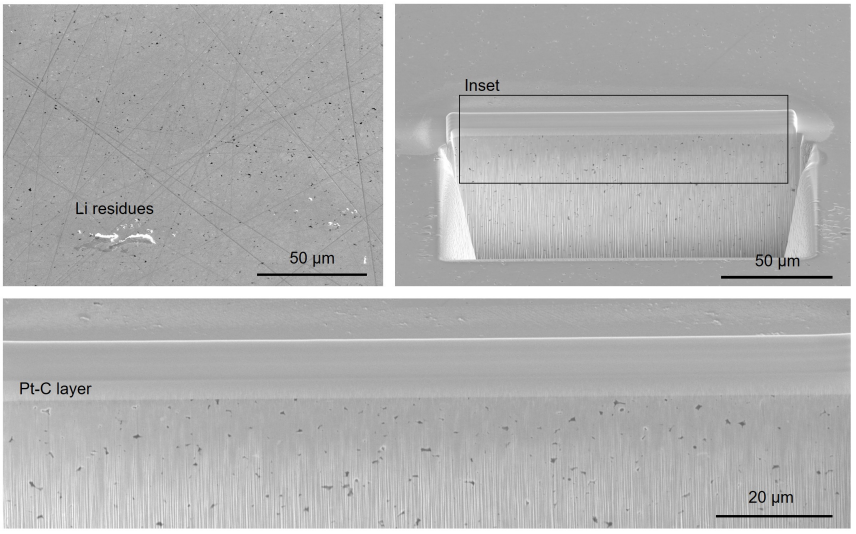


**Supplementary Fig. 8. Surface and cross sectional images of LLZTO after cell assembly**. After assembly of the Li/LLZTO/Li cell and application of a 5 MPa stack pressure, the cell was disassembled and the lithium electrode was peeled off. No surface or subsurface cracks are visible in the LLZTO pellet, suggesting that the LLZTO polishing and cell assembly procedure does not damage the SE.

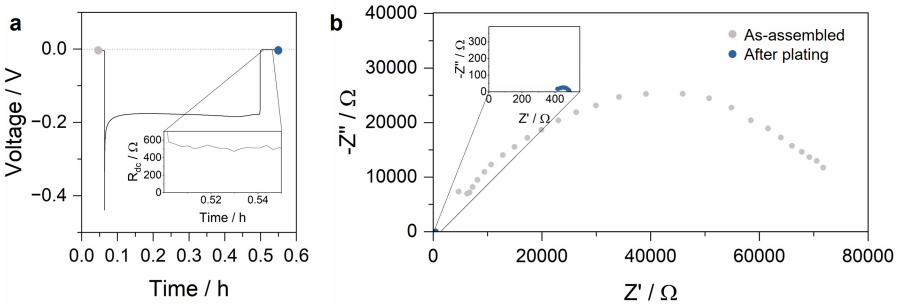


**Supplementary Fig. 9**. **Short-circuited cell for EBIC experiments. a**, Voltage profile of the Li/LLZTO/Li cell used for the EBIC experiment. A short circuit occurred at 0.5 h, after which the cell resistance was around 480 Ω. **b**, Potentiostatic electrochemical impedance spectra of the Li/LLZTO/Li cell before and after the plating step.

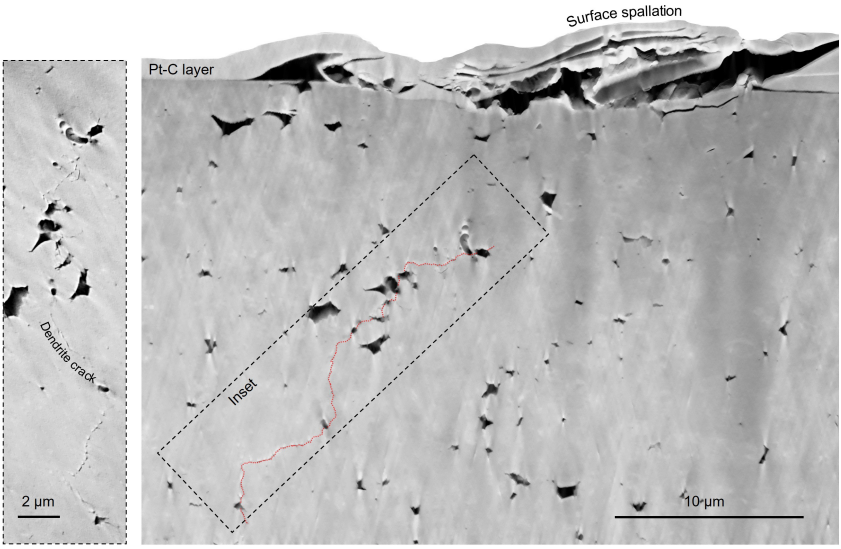


**Supplementary Fig. 10. Cross section of the spallation crack after EBIC.** The plasma-FIB cross section of the surface spallation reveals a thin crack extending into the LLZTO pellet. The image was post-processed to remove the vertical curtaining lines.

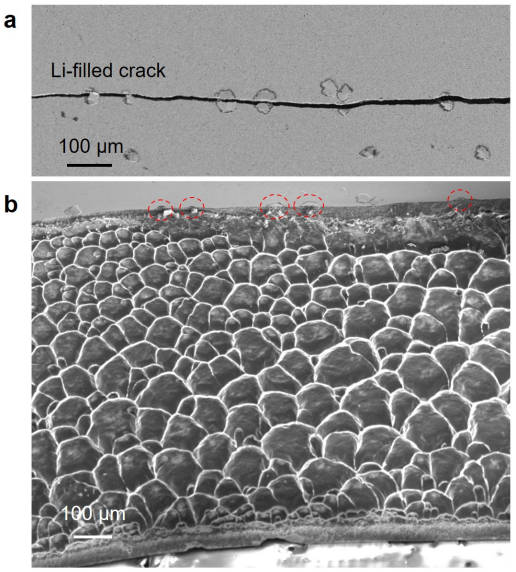


**Supplementary Fig. 11. Macroscopic crack running through the LLZTO pellet. a**, Secondary electron image of the surface of a short-circuited LLZTO pellet. A large crack runs through some surface spallations, suggesting that they represent hot-spots for the focusing of both electrical current density and mechanical stress. It is possible that this crack was ultimately opened by the combined pressure from lithium plating and from the external stack pressure applied to the Li/LLZTO/Li cell. **b**, The pellet was manually cleaved to reveal that the crack is full of lithium. The surface spallations are visible on the top surface (circled).

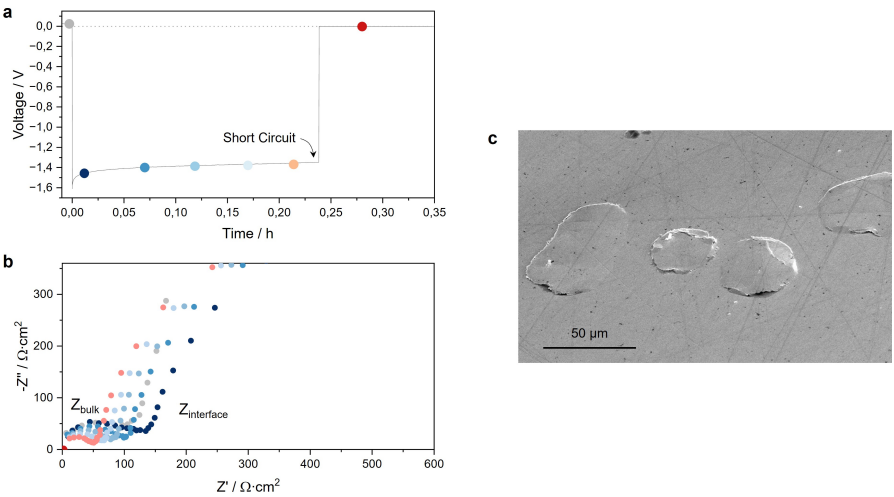


**Supplementary Fig. 12**. **Lithium plating under zero external stack pressure. a**, Voltage profile of a Li/LLZTO/Li cell during plating at 0.5 mA $cm^{-2}$ and zero externally applied stack pressure. **b**, GEIS data collected in operando, showing the decrease in $R_{bulk}$ during plating. **c**, Secondary electron image of the surface of the short-circuited LLZTO pellet after peeling off the plated Li electrode.

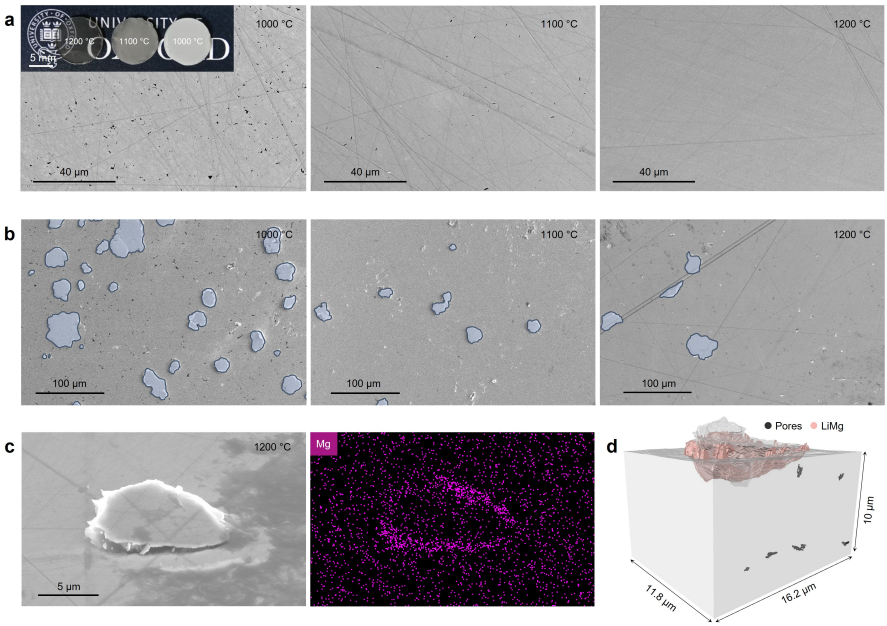


**Supplementary Fig. 13**. **Population density of surface spallation cracks with LLZTO density. a**, Secondary electron images of the surface of LLZTO pellets with different densities. In the inset, photo of pellets showing an increase in transparency with pellet density. **b**, Surface images of the LLZTO surface after plating, showing that as the LLZTO density increases with sintering temperature, the number of surface spallation cracks decreases. **c**, Secondary electron and EDS images and **d**, three-dimensional reconstruction of a spallation crack on a $> 99\%$ dense LLZTO pellet, sintered at 1200 °C. The pellet was assembled with a LiMg-WE, so magnesium could diffuse into the freshly plated lithium in the crack.

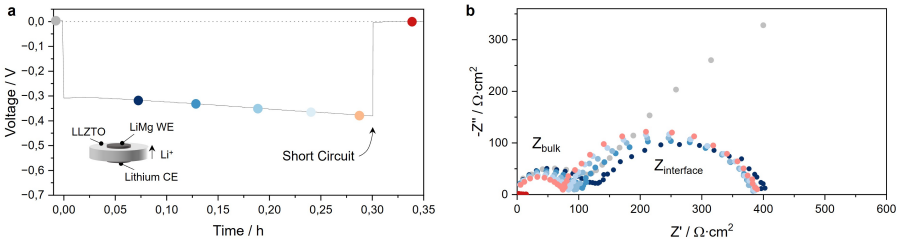


**Supplementary Fig. 14. Lithium plating at the LiMg/LLZTO interface. a**, Voltage profile for a LiMg/LLZTO/Li cell, where lithium is electrodeposited at the LiMg-WE side with a current density of 0.5 mA $cm^{-2}$ and an external stack pressure of 5 MPa. **b**, GEIS data collected in-operando during plating. The behaviour of cells with a LiMg-WE is similar to those with a pure Li-WE, within reasonable variation between different cells.

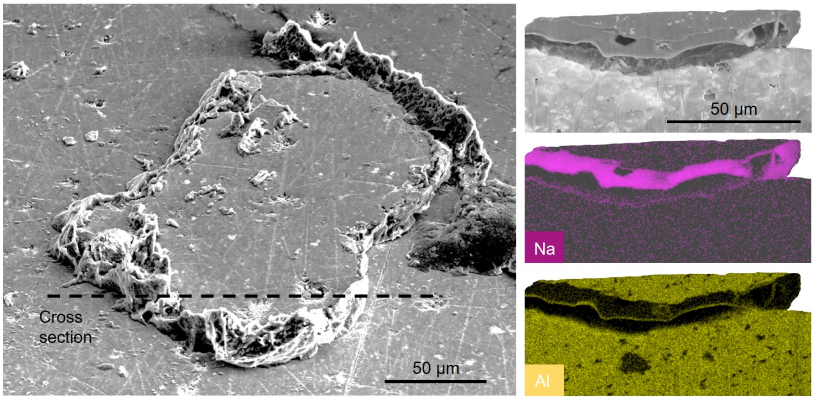


**Supplementary Fig. 15. Spallation crack on the surface of Na $\beta$-$Al_2O_3$. a**, Secondary electron and EDS images of the surface and cross-section of a Na $\beta$-$Al_2O_3$ pellet. The pellet was cycled in a symmetric Na/$\beta$-$Al_2O_3$/Na cell configuration until short-circuit, then the plated Na-WE was peeled off. A large spallation crack is visible where Na metal has plated between the pellet and the fractured surface, similar to the LLZTO behaviour.

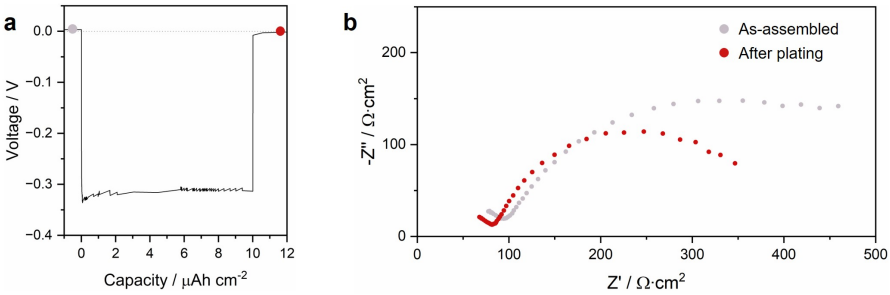


**Supplementary Fig. 16**. **Voltage profile and impedance of a LiMg/LLZTO/Li cell after 10 $\mu$Ah cm$^{-2}$ of lithium plating. a**, Voltage profile of the LiMg/LLZTO/Li cell analysed in Fig. 4a in the manuscript. The cell was cycled at 0.5 mA cm$^{-2}$ and was stopped after only 10 $\mu$Ah cm$^{-2}$ of plated capacity. **b**, Potentiostatic impedance spectra of the LiMg/LLZTO/Li cell before and after the plating step. The $R_{bulk}$ impedance contribution has decreased after plating, but the cell has not fully short-circuited.

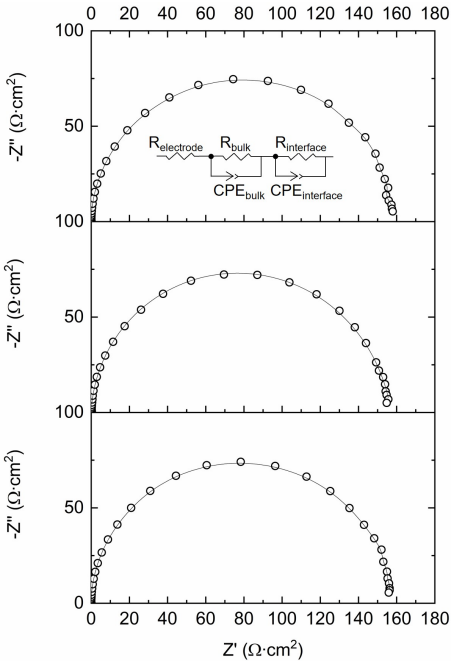


**Supplementary Fig. 17. Starting electrochemical impedance spectroscopy for near-zero $R_{int}$ LLZTO cells.** EIS profiles of the cells used in Fig. 4b in the manuscript and cycled at 0.5, 2.5, and 5 mA $cm^{-2}$ (from top to bottom). The Li/LLZTO interface contribution to the cell impedance is $R_{int} < 6\ \Omega\ cm^{-2}$ for all cells.

**Supplementary Note 1.**

**Serial sectioning of LLZTO for three-dimensional visualization.**

Automated serial sectioning was used to obtain a three-dimensional view of the spallation cracks in the LLZTO pellets. The setup is shown in Supplementary Fig. 18a. The volume of interest was prepared for serial sectioning as follows. Firstly, a Pt-C layer of approximately 5 $\mu$m was deposited to minimize $Xe^+$ beam damage. Secondly, a front trench and side trenches were milled to define the block for serial sectioning. Fiducial markers were then milled next to the volume of interest (Supplementary Fig. 18b and c). Finally, a 30 kV, 15 nA $Xe^+$ beam was used to mill the volume of interest and collect a stack of secondary electron and EDS images of the cross-section, or 'slices' (Supplementary Fig. 18d). The thickness of each slice was 100 nm. Secondary electron imaging was carried out with a 10 kV, 0.8 nA electron beam. This method allowed the capture of microstructural features at the tens of nanometres to the tens of microns scale.

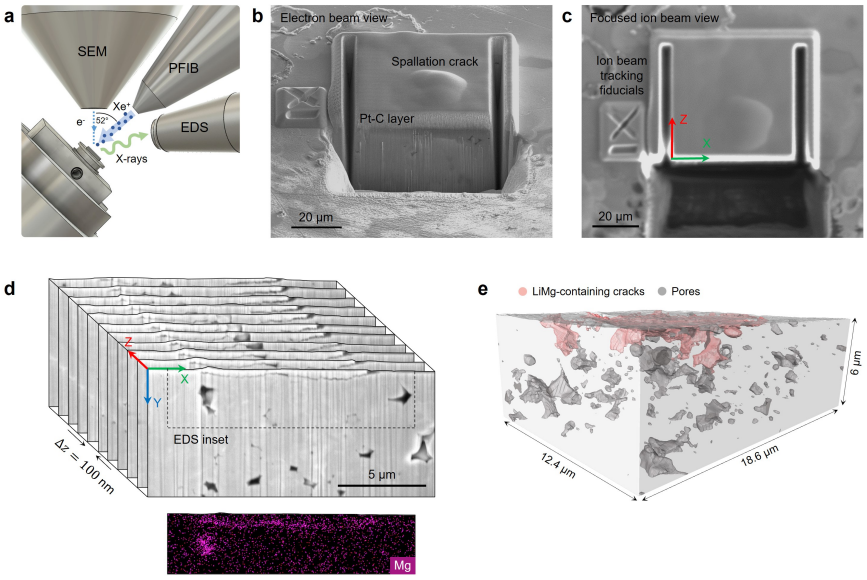


**Supplementary Fig. 18. Automated serial sectioning procedure. a**, Plasma-FIB setup with the sample surface tilted at 52° with respect to the electron beam. The sample stage can be cooled with liquid nitrogen to minimise beam damage. **b**, Electron beam view of the volume of interest. **c**, Plasma-FIB view of the volume of interest. The volume is prepared milling the regions around it with the $Xe^+$ beam, decreasing the milling current in a stepwise manner to obtain a smooth cross-section. **d**, Series of two-dimensional secondary electron and EDS images. **e**, Three-dimensional reconstruction.

The 2D secondary electron images were aligned in sequence to build a three-dimensional view using Avizo 3D (version 2021.2, ThermoFisher Scientific). The y-dimension was corrected to account for the 52° tilt between the electron beam and focused ion beam. The images were then processed by applying a smoothing and noise reduction filter (non-local means filter), as well as a background subtraction to remove brightness variation due to shadowing effects. A Fourier Transform filter was applied to remove the vertical curtaining lines, which are an undesirable surface artefact of FIB milling. The images were then segmented with a semi-automated process to distinguish pores and cracks from bulk LLZTO. Specifically, a thresholding method was used to mark regions of interest, after which a watershed algorithm was applied. EDS images were then consulted to identify the cracks and pores with an above-average magnesium signal. Finally, the 3D reconstruction was obtained (Supplementary Fig. 18e).